Check for updates

Construction of a nanozyme composite drug delivery system based on columbianadin for inflammatory bowel disease therapy

Yanping Zhang,†[a] Hong Xi,[a] Dongyuan Qin,[a] Ping Cao,[a] Shuo Yang,†[b] Jing Yin,†[c] Tianliang Li [ID] *[d] and Lili Ding*[a]

Inflammatory bowel disease (IBD) is characterized by chronic gastrointestinal inflammation driven by oxidative stress and immune dysregulation. This study develops a novel oral nanozyme composite drug delivery system (MXene/CBN@GelMA, MCG) designed for targeted therapy of IBD. The composite integrates antioxidative MXene nanosheets and anti-inflammatory columbianadin (CBN) into a gelatin methacryloyl (GelMA) hydrogel, enabling targeted delivery and therapy. MCG efficiently scavenges reactive oxygen species (ROS) and generates oxygen (O_2) through a superoxide dismutase (SOD)-catalase (CAT) cascade reaction, thereby alleviating oxidative stress and mitigating hypoxia in the inflamed tissues. In a dextran sulfate sodium (DSS)-induced IBD model, MCG treatment significantly reduced disease activity, restored colon length, preserved mucosal integrity, and suppressed pro-inflammatory pathways. Transcriptomic analysis revealed that MCG reversed IBD-associated gene expression dysregulation and modulated immune-related pathways. The system demonstrated high biocompatibility and effective targeting, providing a synergistic therapeutic strategy for IBD through antioxidative and anti-inflammatory mechanisms.

1. Introduction

Inflammatory bowel disease (IBD) is a kind of immune-related disorders characterized by chronic inflammation of the gastrointestinal tract, primarily classified into ulcerative colitis (UC) and Crohn's disease (CD).[1,2] Common clinical manifestations include abdominal pain, diarrhea, and fatigue, and may be accompanied by systemic manifestations such as fever and anemia.[3] Although the exact etiology remains incompletely elucidated, it is widely acknowledged that the pathogenesis of IBD involves multiple factors, including genetic susceptibility, immune dysregulation, intestinal microbiota imbalance, and environmental factors.[4] During IBD-associated pathological processes, excessive production of reactive oxygen species (ROS) and subsequent oxidative stress are considered crucial drivers of sustained inflammation.[5,6] High level of ROS not only directly causes damage to the intestinal structure but also activates

multiple pro-inflammatory signaling pathways, creating a vicious cycle that significantly compromises the efficacy of conventional therapeutics and may even lead to treatment failure.[7] Current clinical management still largely relies on anti-inflammatory drugs, such as corticosteroids and amino-salicylates, which are often associated with considerable side effects including immunosuppression, increased infection risk, and renal toxicity.[8] Therefore, developing novel treatment strategies that actively respond to the high-ROS microenvironment and ameliorate inflammatory responses holds significant clinical relevance and research value.

The emergence of nanomedicine has provided novel perspectives for the treatment of IBD. Nanozymes, nano-materials with intrinsic enzyme-like catalytic activities, have attracted considerable attention owing to their unique combination of the structural functionalities of nanomaterials and the catalytic properties of natural enzymes.[9,10] Compared to conventional natural enzymes, such as superoxide dismutase (SOD) and catalase (CAT) nanozymes, which are prone to denaturation and activity loss under physiological stress (*e.g.*, pH variation and proteolytic degradation). Furthermore, nano-zymes exhibit superior stability, lower production costs, and scalable manufacturability. In contrast to ordinary nano-materials, such as gold nanoparticles (AuNPs) or silica nano-particles (SiO_2 NPs), which generally lack intrinsic catalytic activity. Nanozymes demonstrate specific enzyme-mimicking functions, particularly antioxidant activities resembling those

[a]Shanxi Bethune Hospital, Shanxi Academy of Medical Sciences, Third Hospital of Shanxi Medical University, Tongji Shanxi Hospital, Taiyuan, 030032, China. E-mail: dinglili@sxbqeh.com.cn

[b]Peking University Shenzhen Hospital Department of Gastroenterology, No. 1120 Lianhua Road, Futian District, Shenzhen, 518036, China

[c]Department of Pharmacology, School of Basic Medical Science, Shanxi Medical University, Jinzhong, China

[d]Department of Biomedical Engineering, National University of Singapore, 117583, Singapore. E-mail: biev151@visitor.nus.edu.sg

† These authors contributed equally to this work.

of SOD and CAT.[11] These nanozymes can efficiently scavenge ROS, break the vicious cycle of oxidative stress and offer a promising therapeutic strategy for IBD.

Columbianadin (CBN), a natural coumarin derivative, possesses notable anti-inflammatory and antioxidant capabilities. Investigations into its application in IBD models have revealed promising therapeutic potential. Developing a delivery system based on CBN that enables colon-specific targeting, enhances drug stability, and synergistically modulates the pathological microenvironment is crucial for improving its therapeutic efficacy.[12]

Oral nano-delivery systems represent an ideal platform for achieving colon-targeted drug delivery.[13,14] Their advantages lie in the ability to protect active pharmaceutical ingredients from degradation in the gastrointestinal tract, leverage the enhanced permeability and ELVIS (Extravasation through leaky vasculature and subsequent inflammatory cell-mediated sequestration) effect at sites of colonic inflammation for passive targeting, and enable intelligent controlled release within the diseased colon through the design of carriers responsive to pH, ROS, or enzymes.[15,16] Such capabilities contribute to increased local drug concentrations and reduced systemic side effects.[17] Among various biomaterials, hydrogel microspheres—exemplified by gelatin methacryloyl (GelMA), are regarded as excellent platforms for tissue engineering and drug delivery owing to their highly hydrated nature, tunable structural properties, and favorable biocompatibility.[18]

Based on this rationale, this study develops a nanozyme-based composite drug delivery system. CBN was encapsulated into MXene-based nanozymes, aiming to harness both the high catalytic efficiency of the nanozyme and the anti-inflammatory effects of the natural compound, thereby achieving dual synergistic therapeutic effects. The resulting complex was further encapsulated within GelMA hydrogel microspheres. This integrated system (MXene/CBN@GelMA, MCG) is designed to reliably traverse the highly acidic gastric environment and the near-neutral intestinal conditions, and subsequently respond to the highly ROS-enriched pathological microenvironment of inflamed colon, enabling targeted release for IBD therapy (Scheme 1). The constructed MCG combines "cascade catalytic reactions" and "therapeutic drug function" in a multifunctional system, which exhibits synergistic enhancement in both antioxidant and anti-inflammatory activities, achieving a therapeutic outcome greater than the sum of its parts ("1 + 1 > 2"). This strategy offers a potential and promising approach for the treatment of IBD.

2. Materials and methods

2.1. Experimental materials

Titanium aluminum carbide (MAX phase, Ti_3AlC_2), sodium hydroxide (NaOH), dimethyl sulfoxide (DMSO), lithium fluoride (LiF), 3,3′,5,5′-tetramethylbenzidine (TMB), gelatin, and methacrylic anhydride (MA) were purchased from Shanghai Aladdin Biochemical Technology Co., Ltd. Hydrogen peroxide (H_2O_2) and concentrated sulfuric acid (H_2SO_4) were obtained from Sinopharm Chemical Reagent Co., Ltd. The superoxide dismutase (SOD) assay kit (S0101) was acquired from Beyotime Biotechnology. All chemicals were of analytical grade and used without further purification. Ultra-pure water (18.2 MΩ cm) from a Milli-Q water purification system was used in all experiments.

2.2. Experimental instruments

Transmission electron microscopy (TEM) and EDS mapping images were captured using a Tecnai G2 F20 TWIN (FEI, USA) at 200 kv. Samples were drop-cast onto carbon-coated copper grids
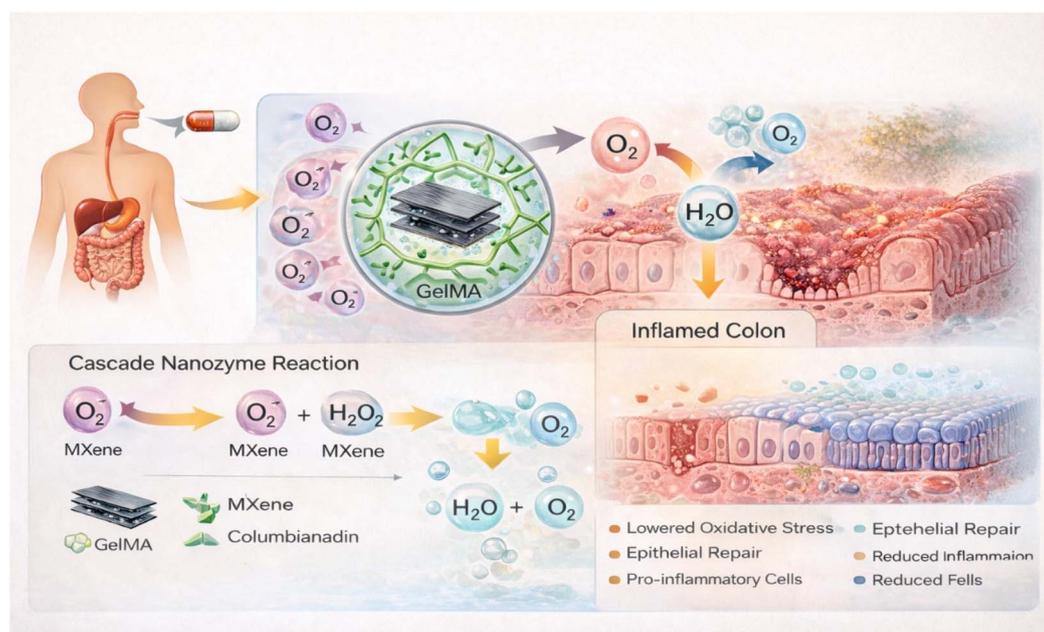
Scheme 1 Construction of nanozyme composite drug delivery system based on columbianadin for inflammatory bowel disease therapy.

and air-dried before imaging. Scanning electron microscopy (SEM) was performed on a GEMINI 300 field-emission microscope (Zeiss, Germany). UV-Vis absorption spectra were recorded on a Lambda 750 spectrophotometer (PerkinElmer, USA). X-ray photoelectron spectroscopy (XPS) was conducted using a Kratos Axis Ultra DLD instrument (Kratos Analytical, UK). X-ray diffraction (XRD) patterns were obtained using a Bruker AXS D2 diffractometer (Bruker, Germany). Cellular images were acquired with an FV 3000 confocal microscope (Olympus, Japan). Dissolved oxygen levels were measured using a Leici dissolved oxygen meter.

2.3. Preparation and characterization of GelMA

2.3.1. Synthesis of GelMA hydrogel. GelMA was synthesized based on a previously reported method with slight modifications. Briefly, 10 g of gelatin (Type A, porcine skin) was gradually dissolved in 100 mL of pre-warmed phosphate-buffered saline (PBS, pH 7.4) at 50 °C under magnetic stirring at 500 rpm until a homogeneous transparent solution was obtained. Then, 0.45 mL of methacrylic anhydride (MA) was slowly added dropwise under continuous stirring to avoid localized high concentration and ensure efficient reaction. The reaction was maintained at 50 °C for 4 hours to achieve methacryloylation of amino groups on gelatin. After reaction, the mixture was transferred into a dialysis bag (molecular weight cutoff: 10 kDa) and dialyzed against deionized water for 7 days at 37 °C, with water changes every 8 hours. The dialyzed solution was frozen at −80 °C for 3 hours and lyophilized at −55 °C for 48 hours to obtain a white porous GelMA powder, which was stored dry and protected from light at −20 °C.

2.3.2. Characterization of GelMA hydrogel

2.3.2.1. Gelation process. To verify the gelation capability, 10% (w/v) GelMA was dissolved in PBS containing 0.25% (w/v) photoinitiator lithium phenyl-2,4,6-trimethylbenzoylphosphinate (LAP). The precursor solution was filtered, injected into 1.5 mL EP tubes, and crosslinked under UV light (365 nm, 10 mW cm^{-2}) for 60 seconds. The gelation was confirmed by inverting the tubes.

2.3.2.2. Swelling ratio test. Lyophilized GelMA discs (diameter: 10 mm; thickness: 2 mm) were weighed (W_d) and immersed in PBS at 37 °C. At designated time points (2, 6, 12, 24, 48, and 72 h), samples were removed, gently blotted, and weighed (W_s). The swelling ratio was calculated as ($W_s − W_d$)/W_d × 100%.

2.3.2.3. Degradation test. Hydrogel degradation was evaluated in PBS containing collagenase II (2 U mL^{-1}). The remaining mass was measured at the same time points to calculate the mass retention rate.

2.3.2.4. Morphological characterization. Lyophilized GelMA hydrogels were swollen in PBS for 24 h, frozen at −80 °C, and lyophilized. Samples were sputter-coated with gold and observed under SEM at 5 kV.

2.3.2.5. Preparation of hydrogel microspheres. GelMA microspheres were fabricated using a microfluidic device. The aqueous phase contained 10% (w/v) GelMA and 0.25% LAP in PBS. The oil phase consisted of paraffin oil with 2% Span 80.

The inner and outer flow rates were set to 50 μL min^{-1} and 200 μL min^{-1}, respectively. The emulsion was UV-crosslinked (365 nm, 8–10 mW cm^{-2}, 60 s), washed with PBS, and collected.

2.4. Synthesis of MXene

Initially, 1.525 g LiF was slowly added to 15 mL of 9 M hydrochloric acid, followed by ultrasonic dispersion for 15 min. Under continuous stirring, 0.75 g MAX phase precursor powder was introduced in batches. After stirring for 1 min, the reaction proceeded at 50 °C for 24 h to complete the etching process. The resulting product was repeatedly washed with copious deionized water until a neutral pH (≈7) was achieved. The suspension was then centrifuged at 8000 rpm for 5 min to collect the precipitate, which was subsequently freeze-dried to obtain crude MXene.

To further exfoliate few- or single-layer MXene, the crude product was dispersed in DMSO and stirred continuously for 24 h. The mixture was then centrifuged at 4500 rpm for 5 min. The collected precipitate was washed multiple times with deionized water, redispersed in deionized water, and purged with high-purity argon for 30 min to remove dissolved oxygen and prevent oxidation. The dispersion was sonicated for 2 h and centrifuged again at 4500 rpm for 1 h. The supernatant was collected and freeze-dried to obtain few- or single-layer MXene solid samples.

2.5. Preparation of MXene/CBN

A one-step method was employed to synthesize the MXene/CBN nanocomposite. Briefly, 0.5 g layered MXene powder was dissolved in 50% (v/v) ethanol and subjected to ultrasonication to achieve uniform dispersion. Then, 0.05 g of CBN powder was added, and the mixture was stirred at 1000 rpm for 24 hours in the dark to enhance the physical interaction and surface synergy between MXene and CBN. After the reaction, the mixture was centrifuged at 4500 rpm for 5 min to collect the crude product, which was washed three times with deionized water. The final MXene/CBN composite was obtained after freeze-drying.

2.6. Fabrication of MCG

To construct the nano-composite hydrogel system, 1.0 g GelMA was weighed and dissolved in 10 mL of sterile phosphate-buffered saline (PBS, pH 7.4) preheated to 37 °C. The solution was magnetically stirred in a constant-temperature water bath until a homogeneous transparent solution was formed. Then, 0.2 g of MXene/CBN nanomaterial mixture was slowly added to the GelMA solution. The mixture was dispersed using a probe-type sonicator (200 W, pulse mode: 2 s on and 3 s off) in an ice bath for 15 min to obtain a well-dispersed GelMA nanocomposite precursor.

The resulting composite system was subsequently processed into structurally stable hydrogel microspheres *via* a microfluidic chip. A polydimethylsiloxane (PDMS)-based microfluidic chip (channel width ≈ 200 μm) was used. The GelMA–MXene/CBN composite solution was continuously injected as the mobile phase, along with 0.25% (w/v) photoinitiator lithium phenyl-

2,4,6-trimethylbenzoylphosphinate (LAP). The system was exposed to 365 nm ultraviolet light (10 mW cm^{-2}) to achieve rapid photochemical crosslinking, resulting in *in situ* formation of spherical or micro-rod-shaped hydrogel structures.

2.7. Evaluation of SOD-like activity of MCG

The SOD-like activity was assessed using a commercial SOD assay kit (Beyotime). The procedure was performed as follows:

Preparation of WST-8/enzyme working solution: a WST-8/enzyme working solution was prepared by thoroughly mixing 151 μL of SOD detection buffer, 8 μL of WST-8 solution, and 1 μL of enzyme solution per 160 μL reaction system. An appropriate volume of the working solution was prepared according to the number of samples.

Preparation of reaction starter working solution: the 40X reaction starter solution was thawed and mixed well, then diluted by adding 1 μL of the starter to 39 μL of SOD detection buffer.

Measurement: the reaction starter working solution was incubated with different concentrations of MCG (final concentrations: 0, 10, 50, 100, 200, and 500 μg mL^{-1}) at 37 °C for 30 min. The absorbance was measured at 450 nm, and the SOD enzyme activity was calculated accordingly.

2.8. Evaluation of CAT-like activity of MCG

The CAT-like activity was determined by measuring oxygen generation using a dissolved oxygen meter. Measurements were performed in PBS (pH 7.4) containing MCG (200 μg mL^{-1}).

Kinetic assays were carried out at room temperature in 1.5 mL of reaction buffer (0.1 M PBS, pH 7.4).

To evaluate the effect of H_2O_2 concentration, reaction systems (1.5 mL) containing H_2O_2 at final concentrations of 0, 0.1, 0.2, 0.3, 0.5, 1, 1.5, and 2 M were prepared. O_2 solubility was monitored for 10 min using a dissolved oxygen meter.

To assess the effect of MCG concentration, 1.5 mL of MCG solutions at different concentrations (0, 10, 50, 100, 200, and 500 μg mL^{-1}) were added to 1.5 mL reaction systems containing 0.5 M H_2O_2. O_2 solubility was monitored over 600 s.

3. Results and discussion

3.1. Construction of the MCG composite system

Few-layer $Ti_3C_2T_x$ MXene nanosheets were successfully exfoliated from a MAX phase precursor (Ti_3AlC_2) *via* a conventional hydrofluoric acid (HF) etching method. The morphology of the obtained MXene nanosheets was examined using TEM. The MXene exhibited a characteristic two-dimensional, transparent, veil-like structure with slightly curled edges, indicating excellent flexibility and ultrathin thickness. EDS elemental mapping confirmed the presence of four elements within the MXene structure: C, O, F, and Ti. These results not only reflect effective elemental inheritance from the precursor but also attest to the successful preparation of MXene (Fig. 1A).[19]

On the basis of successfully synthesized MXene nanosheets, the hydrophobic drug CBN was loaded onto the MXene surface through physical adsorption and π–π stacking interactions, resulting in the formation of the MXene/CBN composite. As shown in Fig. 1B, drug aggregates were observed at the edges of
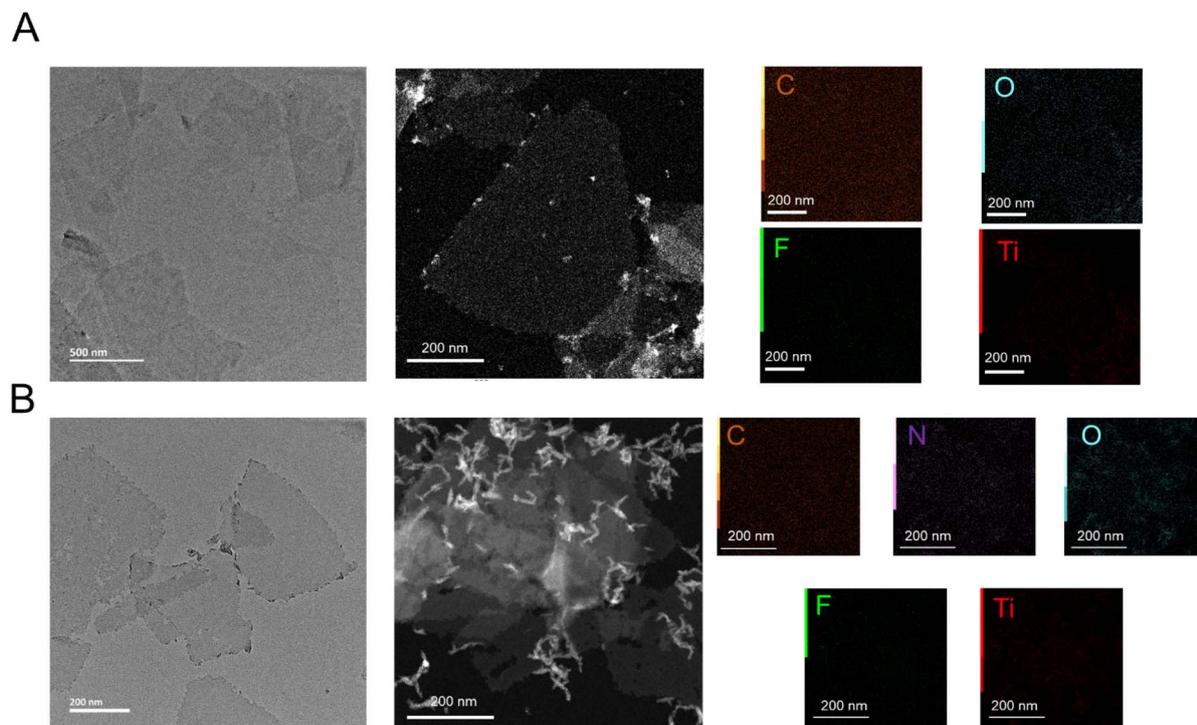

Fig. 1 The characteristic of MXene and MXene/CBN. (A) The TEM and mapping of MXene. Scale bar: 500 and 200 nm. (B) The TEM and mapping of MXene/CBN. Scale bar: 200 nm.

MXene, while CBN was uniformly distributed across the nano-sheet surfaces and exhibited a spindle-like morphology under electron microscopy. EDS elemental mapping confirmed the presence of five elements: C, N, O, F, and Ti in the MXene/CBN composite. The detection of nitrogen, which originates exclusively from CBN, provides clear evidence for the successful loading of CBN onto MXene.

Subsequently, the MXene/CBN composite was uniformly dispersed in a GelMA prepolymer solution. In the presence of the photo initiator LAP, crosslinking polymerization between GelMA molecular chains was initiated by irradiation with 405 nm blue light, ultimately forming a three-dimensional network that securely encapsulated the MXene/CBN composite, yielding the MCG composite hydrogel. The synthesis scheme and process were illustrated in Fig. 2A and B.

Further swelling performance tests were conducted on the GelMA hydrogel (Fig. 2C). The MXene/CBN nanocomposite was first prepared before incorporation into GelMA to promote uniform dispersion, maximize the synergistic antioxidant activity, and enable more controlled release, rather than simply loading MXene and CBN together in a single step. Experimental results indicated that the swelling ratio of the GelMA hydrogel
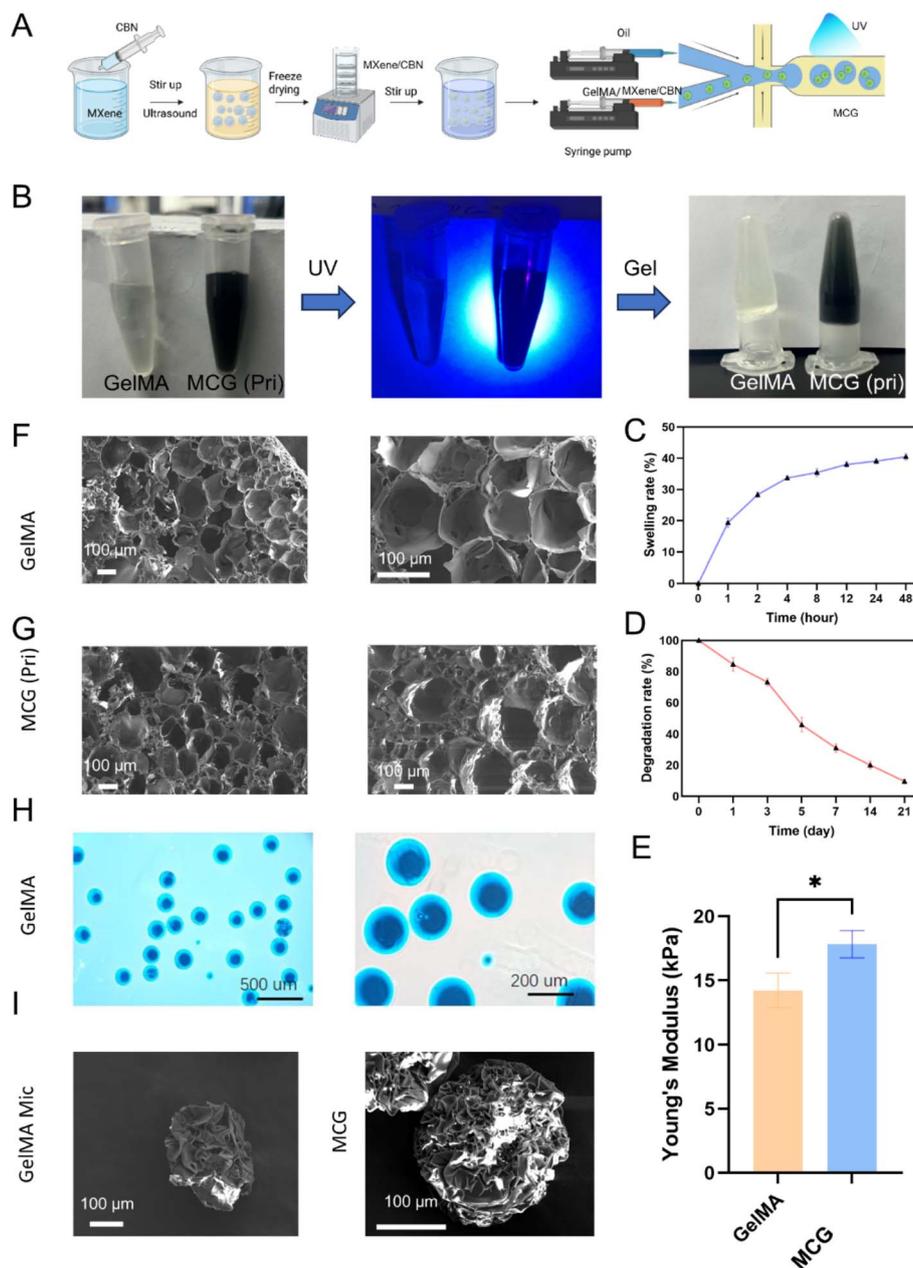

Fig. 2 The characterization of MCG. (A) The synthesis of MCG. (B) GelMA hydrogel and MCG hydrogel (MCG Pri) process. (C) GelMA hydrogel swelling performance test. (D) GelMA hydrogel degradation performance test. (E) Mechanical strength of GelMA hydrogel. (F) SEM image of GelMA hydrogel, scale bar: 100 μm. (G) SEM image of MCG hydrogel, scale bar: 100 μm. (H) Actual image of hydrogel microspheres, scale bar: 500 and 200 μm. (I) GelMA and MCG hydrogel microspheres, scale bar: 100 μm. Data are presented as mean $\pm$ SD, $n = 3$, ns: $p > 0.05$, *$p < 0.05$.

increased gradually over time. Within 48 h, the swelling ratio reached its maximum value, demonstrating the favorable water absorption capacity of the hydrogel, which is of significant importance for its application in drug delivery systems. The high swelling ability enables the hydrogel to carry substantial drug loads and facilitates drug release through hydration *in vivo*. These findings suggest that the GelMA hydrogel possesses excellent expansion characteristics in solution, making it suitable for long-term drug release and tissue engineering applications.

The degradation behavior of the GelMA hydrogel is shown in Fig. 2D. Experimental results revealed that the degradation rate of the GelMA hydrogel decreased progressively over time (Fig. 2D). Within 21 days, the degradation rate slowed significantly, indicating a relatively slow degradation process.

Fig. 2E presents the mechanical strength data of the GelMA hydrogel, indicating a relatively low Young's modulus value, which suggests favorable mechanical compliance and flexibility, as commonly reported for GelMA-based hydrogel systems.[20] This property makes the GelMA hydrogel suitable for tissue engineering applications requiring low stiffness and high ductility. Upon incorporation of the MXene/CBN composite, the resulting GelMA-based hydrogel exhibited a significant improvement in mechanical strength, as reflected by an increased Young's modulus. This enhancement demonstrates that the MXene/CBN composite effectively reinforces the mechanical properties of the hydrogel, supporting the feasibility of modulating GelMA performance through nano-composite integration.

SEM images of the GelMA hydrogel and the MCG composite hydrogel are shown in Fig. 2F and G, respectively. The pure GelMA hydrogel displays a uniformly porous architecture, while the composite hydrogel exhibits a more compact pore structure, indicating improved structural stability owing to the incorporation of the nanocomposite. Under higher magnification, MXene/CBN nanosheets—visible as bright white sheet-like structures—could be clearly observed embedded uniformly within the pore walls of the GelMA matrix without apparent aggregation.[21] This demonstrates the effectiveness of the pre-mixing and photo-crosslinking strategy in preventing nano-sheet agglomeration and achieving homogeneous distribution within the three-dimensional network. The pore architecture of hydrogel plays a critical role in cell growth and drug release behavior, and a more tightly arranged porous structure may facilitate controlled drug release.

Fig. 2H shows a macroscopic view of the hydrogel microspheres. The GelMA hydrogel microspheres exhibit a uniform size distribution with an average diameter of approximately 200 μm, while MCG display even greater uniformity and a similar average size of about 200 μm.[22] These results indicate that the incorporation of the composite material significantly alters the morphological characteristics of the microspheres and further optimizes their physical properties. SEM images of both GelMA and MCG hydrogel microspheres are presented in Fig. 2I. Compared to the pure GelMA microspheres, the composite microspheres show a denser and more compact structure, suggesting improved microsphere stability due to the

composite formation, which may influence their performance in drug delivery applications. These results provide a solid foundation for the subsequent *in vivo* application of the hydrogel microspheres.

The XPS survey spectrum (Fig. 3A and S1) further confirmed the elemental composition, primarily including C 1s, O 1s, F 1s, and Ti 2p, with no significant Al signal detected, reaffirming the completeness of the etching process. Upon loading with CBN, the XPS survey spectrum (Fig. 3B) showed five elemental peaks: C 1s, N 1s, O 1s, F 1s, and Ti 2p (Fig. 3B and S2). The presence of the N 1s peak, originating from CBN, confirms effective binding between the two components. Similarly, the XPS spectrum of the final MCG composite also exhibited these five elemental peaks. Further detailed analysis of the elemental states was conducted using high-resolution XPS spectra (Fig. 3C and S3). High-resolution analysis of the Ti 2p spectrum revealed peaks at binding energies of 454.3 and 455.1 eV, corresponding to the Ti–C bond (Ti^0 $2p_{3/2}$) and Ti(II) $2p_{3/2}$ (*e.g.*, Ti–O or Ti–F_x), respectively, along with intense peaks at 458.5 and 464.2 eV assigned to Ti(IV)–O (Ti $2p_{3/2}$ and $2p_{1/2}$). These diverse surface valence states (Ti^0, Ti^{2+}, Ti^{4+}) form the structural basis for the enzyme-like catalytic activity of MXene (Fig. 3D).

Owing to differences in the zeta potentials of individual components, zeta potential analysis was employed to investigate the interactions between them (Fig. 3E). MXene exhibits a zeta potential of −7.9 mV, which is attributed to its surface functional groups (*e.g.*, –O, –OH, and –F) that carry negative charges. Similarly, CBN shows a zeta potential of approximately −8.0 mV, also resulting from its negatively charged surface groups. The zeta potential of the MXene/CBN composite was measured to be −15.16 mV, indicating successful interaction between CBN and MXene. Ultimately, the MCG nanozyme composite system demonstrates a zeta potential of −25.92 mV. This significant change suggests that GelMA effectively encapsulates the MXene/CBN composite (Fig. 3E).[11]

UV-Vis spectroscopy (Fig. 3F) provided further evidence for the successful formation of the composite from the perspective of optical properties. The MXene nanosheets exhibited a broad characteristic absorption extending into the near-infrared region, which is attributed to their metallic conductivity. Free CBN showed strong absorption peaks near 220 and 340 nm. In the absorption spectrum of the MXene/CBN composite, both the broad peak of MXene and the two characteristic peaks of CBN were observed simultaneously. Notably, the absorption peaks of CBN displayed a slight hyperchromic effect, further indicating successful loading of CBN onto the MXene surface and suggesting electronic interaction between the two components. After encapsulation into GelMA, the entire composite system retained all these characteristic absorption features.[23]

3.2. Investigation of MCG nanozyme cascade reaction

In the previous section, the MCG nanozyme composite system was successfully constructed. This section focuses on evaluating the enzyme-like catalytic activities of the MCG composite, particularly its efficient SOD-CAT cascade activity. The abundant variable valence titanium sites (Ti^{3+}/Ti^{4+}) on the surface of
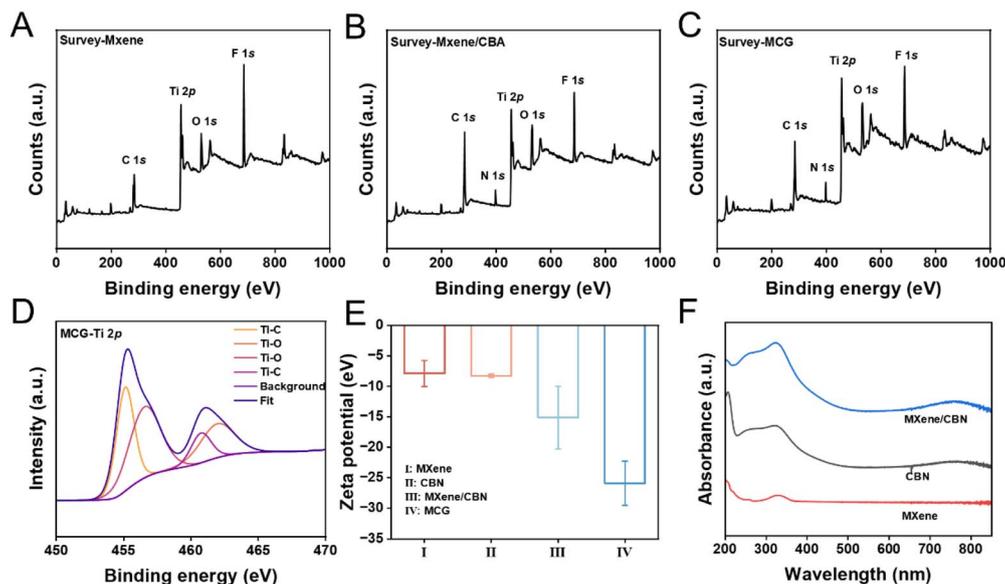
Fig. 3 (A–C) Survey XPS of MXene, MXene/CBN, MCG. (D) XPS high-resolution of Ti 2p of MCG. (E) Zeta potential analysis of MXene, CBN, MXene/CBN, MCG. (F) UV absorption spectra of MXene, CBN, MXene/CBN. Data are presented as mean ± SD, ($n = 3$).

MXene nanosheets serve as the structural foundation for its enzyme-mimetic properties. These active sites facilitate efficient catalysis of various reactive oxygen species (ROS) through reversible redox reactions.[24]

The SOD-like activity involves the specific dismutation of superoxide anion radicals ($O_2^{\bullet-}$) *via* the reaction: $2O_2^{\bullet-} + 2H^+ \rightarrow H_2O_2 + O_2$. The catalytic mechanism entails a refined electron transfer process: first, an $O_2^{\bullet-}$ radical transfers an electron to a low-valence titanium site (Ti^{3+}) on the MXene surface, thereby being oxidized to O_2, while the titanium site is oxidized to a higher state (Ti^{4+}). Subsequently, another $O_2^{\bullet-}$ acquires an electron from the high-valence titanium site and is reduced to H_2O_2 in the presence of protons, accompanied by the reduction of the titanium site. This cyclic mechanism enables MXene to efficiently eliminate $O_2^{\bullet-}$, similar to natural SOD.[25]

The SOD-like activity of the MCG composite was quantitatively assessed using the WST-8 method. The formation of WST-8 formazan was significantly inhibited with increasing concentrations of MCG (Fig. 4A). The calculated IC_{50} value for the SOD-like activity of MCG nanosheets was 55.01 μg mL^{-1}, confirming its efficient $O_2^{\bullet-}$ scavenging capacity and catalytic performance comparable to that of natural SOD enzyme (Fig. 4B). Since H_2O_2 is the product of the SOD-catalyzed reaction, it can serve as a substrate for subsequent CAT-like activity, leading to O_2 generation and enabling a cascade reaction (Fig. 4C). The system further catalyzes the decomposition of H_2O_2, the product of the SOD reaction *via* CAT-like activity ($2H_2O_2 \rightarrow 2H_2O + O_2$). The CAT-like activity also relies on valence changes of titanium sites on the MCG surface. The catalytic process involves adsorption and activation of H_2O_2 molecules, heterolytic cleavage of the O–O bond, and eventual formation of water and O_2 (Fig. 4D). The CAT-like activity was validated by dissolved O_2 assays, where a rapid increase in O_2 concentration was observed after adding the composite to an

H_2O_2 solution. The O_2 generation rate exhibited clear dependencies on both H_2O_2 and MCG concentrations, indicating efficient catalytic decomposition of H_2O_2 (Fig. 4E and F).[26]

These results not only demonstrate the effective removal of $O_2^{\bullet-}$ by MCG (SOD activity), more importantly, reveal that the produced H_2O_2 acts as an intermediate that initiates the CAT reaction: MCG first converts $O_2^{\bullet-}$ into H_2O_2 and subsequently decomposes it into H_2O and O_2, thereby achieving highly efficient clearance of ROS burst. This cascade reaction mimics the endogenous antioxidant enzyme defense system and offers an innovative therapeutic strategy for oxidative stress-related diseases.

In summary, MCG successfully simulates the cascade antioxidant function of natural enzymes through efficient ROS elimination and O_2 generation mechanisms, providing a novel approach for the treatment of IBD.

3.3. Analysis of *in vitro* anti-inflammatory effects of the MCG nanozyme composite system

To evaluate the potential of the nanozyme composite system for biomedical applications, we first assessed the cytotoxicity of MCG extracts at various concentrations on NCM460 cells using the CCK-8 assay. As shown in Fig. S4, compared with the blank control group, the relative cell viability remained above 90% after 1, 3, and 5 days of incubation, even at the highest tested concentration (500 μg mL^{-1} of MCG), with no statistically significant differences observed. The effective incorporation of MXene and CBN was confirmed by loading efficiency measurements (MXene: 78.3%, CBN: 64.5%). These results indicate that the MCG composite system did not exhibit significant cytotoxicity within the tested concentration range, demonstrating favorable biocompatibility and biosafety. This supports its potential use as a biomedical material in
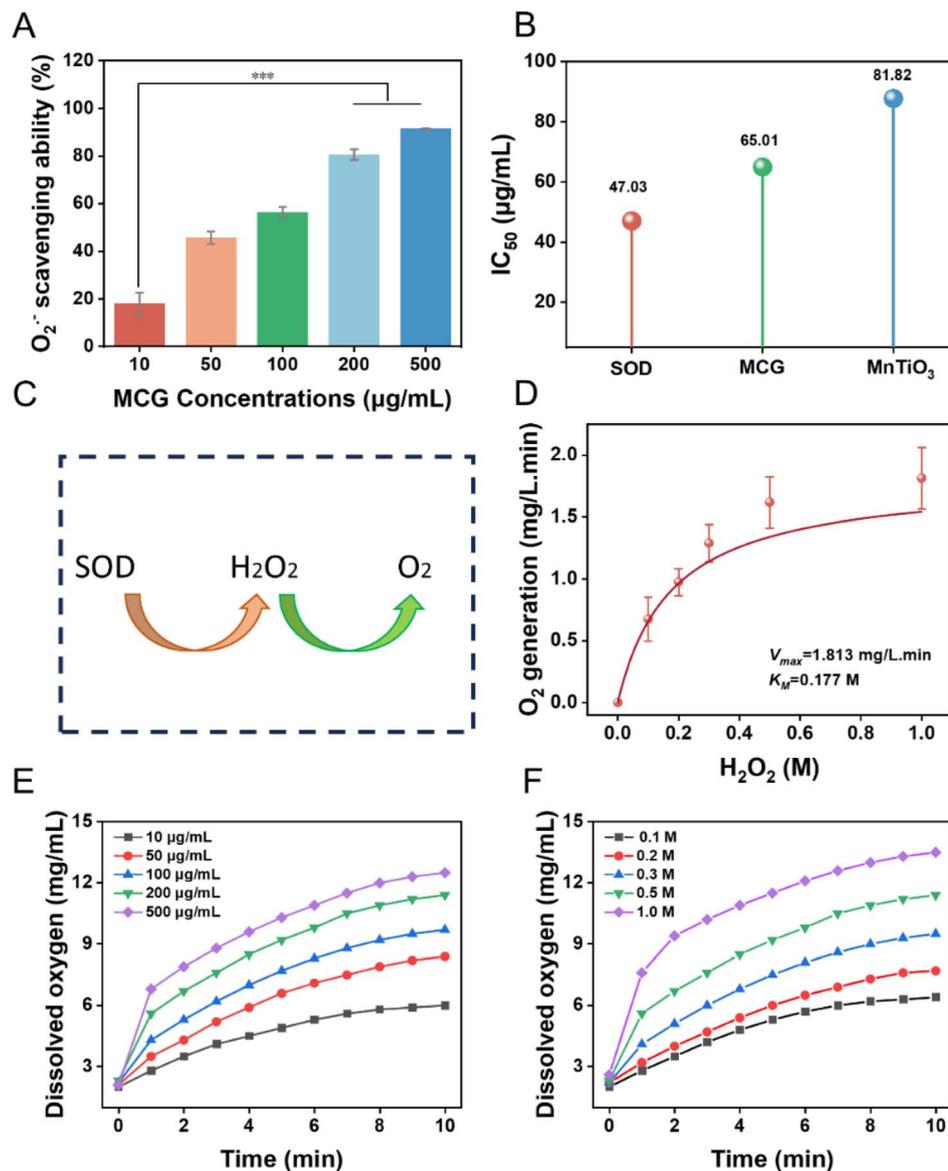
Fig. 4 The performance of SOD–CAT cascade reaction. (A) Exploration of SOD nano-enzyme performance. (B) Comparison of IC_{50} of MCG and natural SOD enzymes. (C) Schematic diagram of SOD–CAT cascade reaction. (D) Kinetic curve of CAT performance. (E) O_2 dissolved by MCG at different concentrations of H_2O_2. (F) O_2 dissolved at different concentrations of MCG.

subsequent anti-inflammatory studies. The high cell viability can be attributed to the inherent biocompatibility of GelMA hydrogel and its effective shielding of potential cell membrane damage induced by MXene nanosheets. GelMA hydrogel, which mitigates the potential cytotoxicity of MXene nanosheets as demonstrated by direct comparison of cell viability between free MXene and MCG (Fig. S5).

To visually verify the antioxidant functionality of the composite system within the intracellular environment, we performed immunofluorescence analysis on DSS-stimulated NCM460 cells using the ROS-sensitive fluorescent probe DCFH-DA and the O_2 probe $Ru(dpp)_3Cl_2$. DCFH-DA is non-fluorescent and can freely cross the cell membrane. Once hydrolyzed by intracellular esterases to DCFH, it reacts with ROS to form highly green-fluorescent DCF. As shown in Fig. 5A,

cells in the IBD + PBS inflammatory model group exhibited intense green fluorescence, indicating substantial ROS generation due to inflammatory stimulation. In contrast, the IBD + MCG group showed significantly reduced green fluorescence intensity, demonstrating that MCG effectively scavenges excess ROS in the inflammatory microenvironment.[11]

It should be noted that DSS stimulation induced nuclear morphology alterations in NCM460 cells, including irregular nuclear contours and disordered spatial arrangement. Such changes have been reported to be associated with oxidative stress-related cellular injury, as excessive ROS may induce DNA damage and chromatin remodeling at early stages of cellular stress. Notably, MCG treatment partially normalized these nuclear features, consistent with its intracellular ROS scavenging effect. These observations suggest that the nuclear
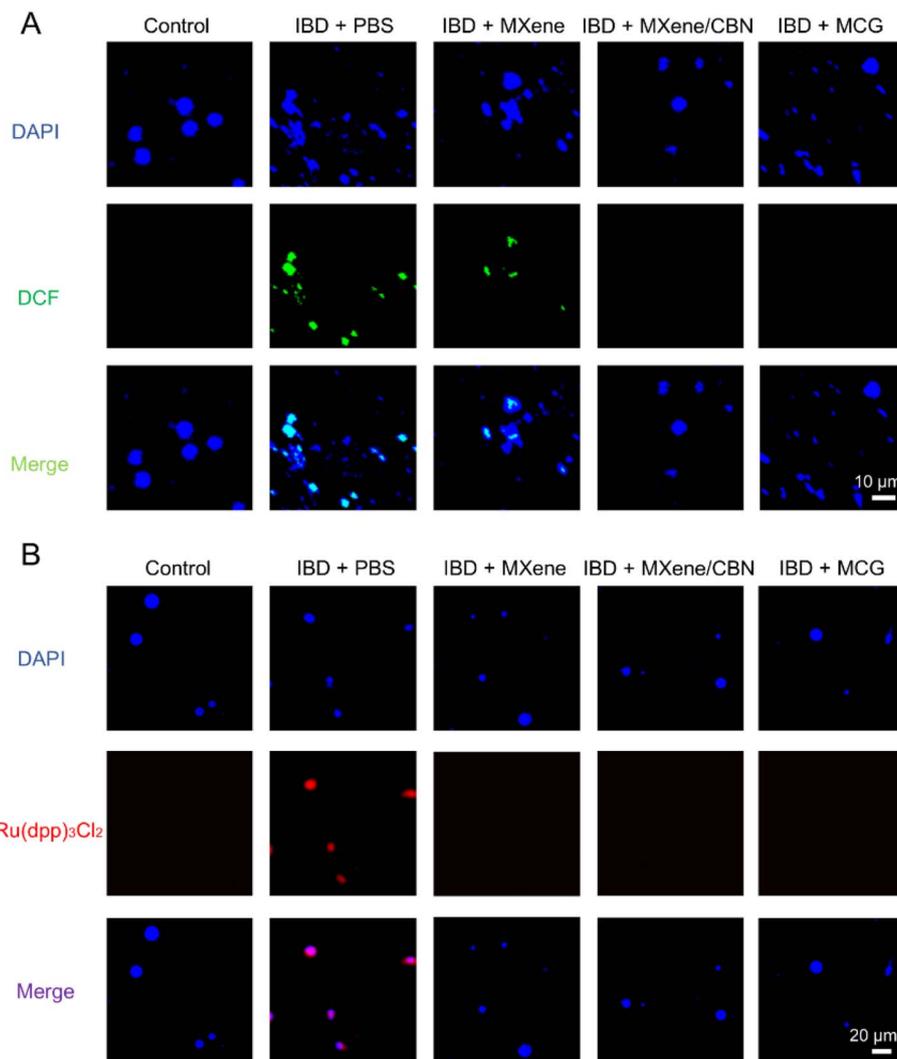
Fig. 5 (A) ROS scavenging in the NCM460 *in vitro* inflammation model under different treatment modalities. Scale bar: 10 μm. (B) O_2 generation in the NCM460 *in vitro* inflammation model under different treatment modalities. Scale bar: 20 μm.

morphology changes are associated with ROS-mediated cellular stress rather than technical artifacts.

Simultaneously, cells were stained with the red fluorescent oxygen probe $Ru(dpp)_3Cl_2$, which is highly sensitive to O_2 concentration. As illustrated in Fig. 5B, no significant red fluorescence signal was detected in the cytoplasm of MCG-treated cells, in clear contrast to the strong red fluorescence observed in the IBD + PBS inflammatory model group. This confirms that the CAT-like activity of MCG successfully catalyzes the decomposition of H_2O_2 and generates O_2 within cells. This outcome is of notable significance: oxygen generation helps alleviate the hypoxic microenvironment commonly found in inflammatory colon regions, thereby indirectly inhibiting pro-inflammatory pathways such as HIF-1α and further enhancing the anti-inflammatory effect.[11,27]

Excessive ROS production during inflammation is a key factor inducing cell apoptosis. These results demonstrate that the MCG composite system, through its synergistic effects—efficient ROS scavenging by the nanozyme to mitigate oxidative damage, combined with the anti-inflammatory function of CBN—effectively blocks ROS-mediated apoptotic signaling pathways, thereby providing robust protection for cells under inflammatory conditions.

3.4. *In vivo* therapeutic efficacy of MCG in IBD treatment

Prior to *in vivo* studies, the targeting capability of the MCG composite system was evaluated. MXene, MXene/CBN, and MCG were labeled with the fluorescent dye ICG and monitored using an *in vivo* imaging system. Following oral administration, the MCG group exhibited strong and persistent near-infrared fluorescence signals specifically localized in the colon region. Even 24 h post-administration, significant fluorescence remained detectable in the colon, while signals in other organs were minimal (Fig. 6). These results indicate that the GelMA hydrogel effectively delivers MXene/CBN to the inflamed colon and enables prolonged retention, establishing a foundation for localized treatment.[28]
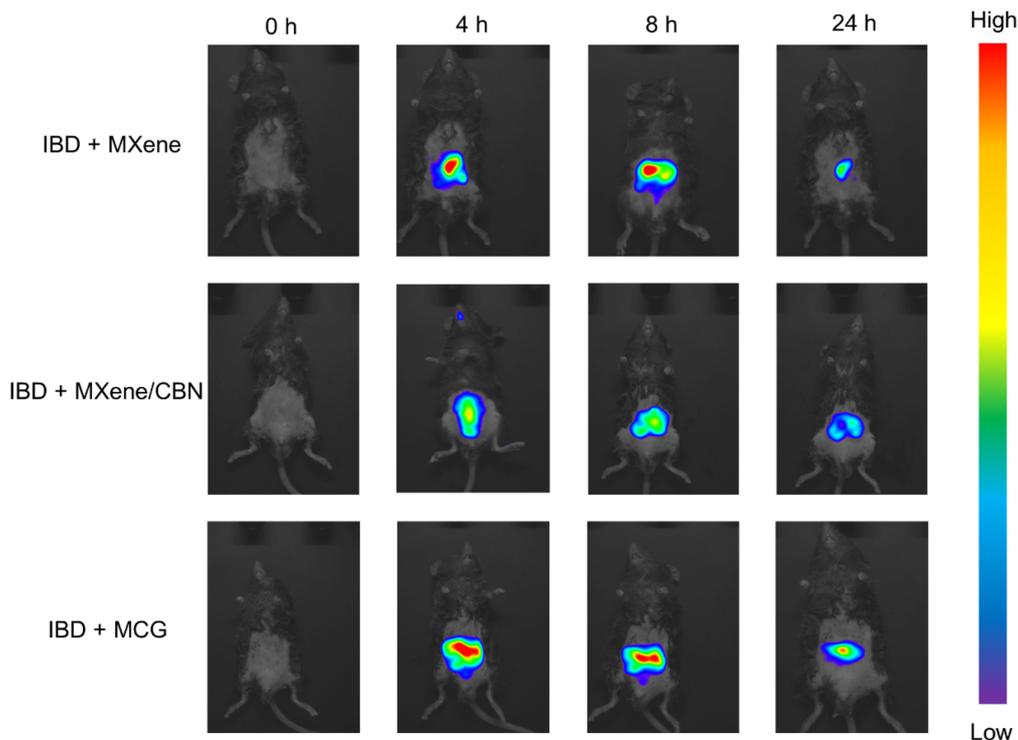
Fig. 6 *In vivo* imaging of mice under different treatment modalities. Different groups: IBD + MXene (23.5 μg mL^{-1}); IBD + MXene/CBN (26.1 μg mL^{-1}); IBD + MCG (200 μg mL^{-1}).

To comprehensively evaluate the therapeutic effect of the MCG nanozyme system on IBD, an acute colitis model was induced in mice using DSS, The mice were randomly divided into five groups ($n = 6$): control, IBD + PBS, IBD + MXene, IBD + MXene/CBN, IBD + MCG.

Body weight, stool consistency, and bloody stool were recorded daily, and the disease activity index (DAI) was calculated. On day 8, the mice were euthanized, and colon tissue along with its contents were collected for further analysis (Fig. 7A).

Colon length serves as an intuitive macroscopic indicator of colonic inflammation. The DSS model group showed significant colon shortening with edema of the intestinal wall. In contrast, the MCG treatment group exhibited the best recovery in colon length, comparable to the control group and significantly longer than both the IBD + MXene and IBD + MXene/CBN groups, indicating its superior efficacy in alleviating inflammation and tissue edema (Fig. 7B and C).[29]

Furthermore, MCG effectively ameliorated DSS-induced weight loss (Fig. 7D). The DAI, a core metric for evaluating colitis severity, increased rapidly in the DSS model group, reflecting substantial weight loss, severe diarrhea, and evident bloody stools. All treatment groups showed varying degrees of symptom relief, with the MCG group demonstrating the most pronounced therapeutic effect. From day 3 onward, the DAI score of the MCG group was significantly lower than that of the model group and other treatment groups (Fig. 7E). As shown in Fig. S6 and S7, the DSS-induced IBD model group exhibited a significant increase in serum FITC-dextran levels compared with the control group, indicating severe intestinal barrier disruption. MCG treatment significantly reduced serum FITC-dextran levels in a dose-dependent manner. Furthermore, after treating with MCG, TNF-α and IL-6 levels were decreased by approximately 50%. These results indicate that MCG effectively restores intestinal mucosal integrity in IBD mice in a dose-dependent manner.

Histopathological analysis of colon tissues from each group is presented in Fig. 8A. The DSS model group exhibited severe mucosal structural destruction, significant crypt loss, a dramatic reduction in goblet cells, and extensive inflammatory cell infiltration. The MXene and MXene/CBN treatment groups showed only mild improvement. In contrast, the MCG treatment group displayed substantial recovery: the mucosal structure remained largely intact, crypt morphology was nearly normal, inflammatory cell infiltration was markedly reduced, and the histopathological score was significantly lower than those of the model and other treatment groups. Abundant restored goblet cells and a continuous mucus layer were observed in the MCG group, with significantly higher mucin-positive area compared to the model group, indicating a strong ability to promote mucosal barrier repair and regeneration—a critical factor in IBD treatment.[30]

Major organs including the heart, liver, spleen, lungs, and kidneys were collected for histological examination to assess biosafety. As shown in Fig. 8B, no obvious pathological changes were observed in the IBD + MXene, IBD + MXene/CBN, or IBD + MCG groups, and all were consistent with the control group, confirming the high biosafety of all three materials.
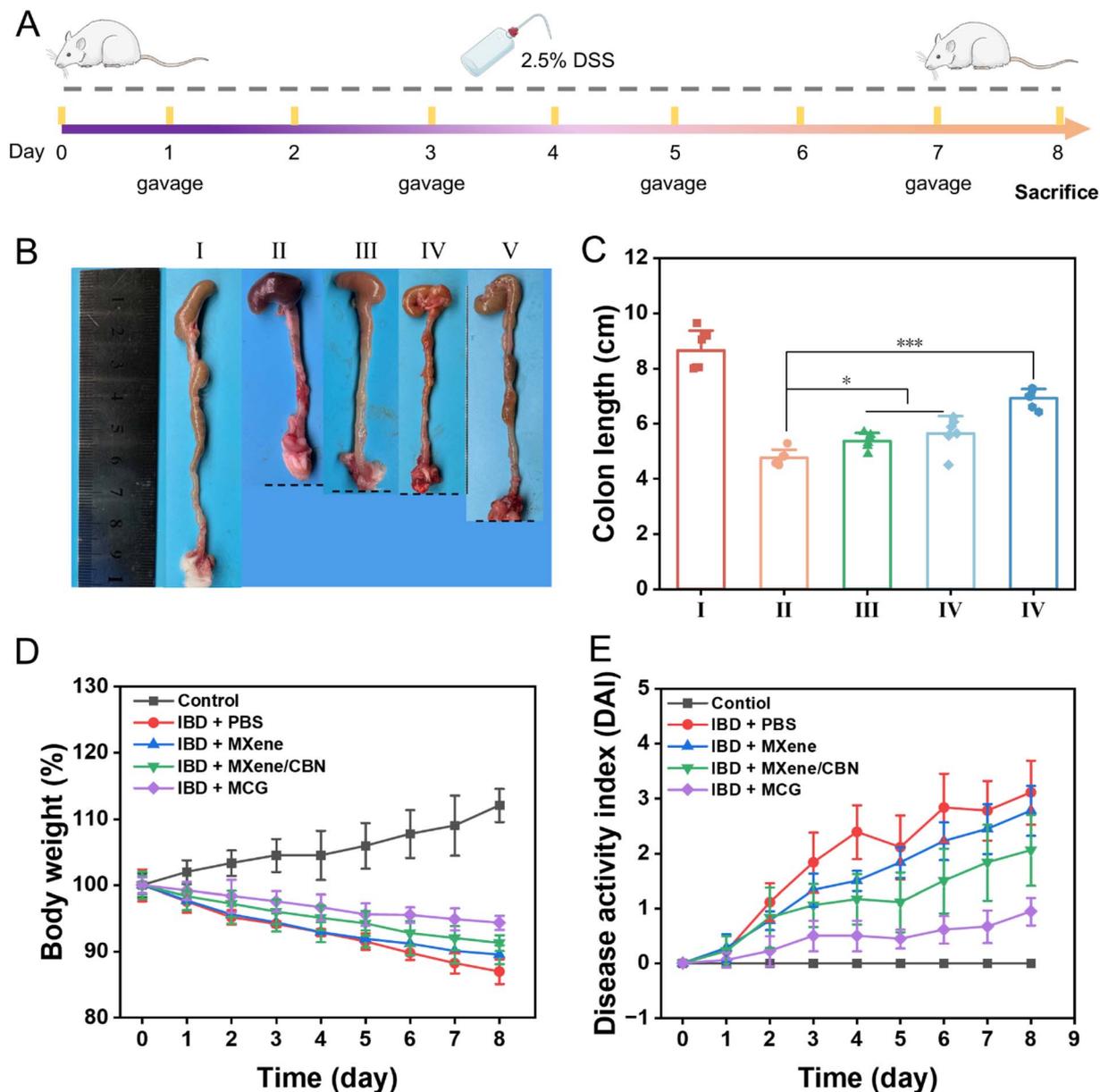
Fig. 7 (A) Scheme of experimental design. Acute experimental colitis in mice was induced by giving 2.5% (w/v) DSS and treated with PBS, MXene, MXene/CBN, MCG on day 1, 3, 5 and 7, with sacrifice on day 8. (B) Representative images of mice colons following different treatments. (C) Statistical analysis of colon length across groups using one-way ANOVA. (D) Body weight changes. (E) Disease Activity Index (DAI) scores, with statistical analysis on Day 8. Data are presented as mean ± SD, $n = 6$, ns: $p > 0.05$, *$p < 0.05$, **$p < 0.01$, ***$p < 0.001$. I: Control, II: IBD + PBS, III: IBD + MXene, IV: IBD + MXene/CBN, V: IBD + MCG.

3.5. Transcriptome sequencing analysis

To further elucidate the mechanism of action of the MCG composite system in IBD at the genomic level, total RNA sequencing (RNA-Seq) was performed on colon tissues from each experimental group. Bioinformatics analysis was systematically applied to identify and interpret differentially expressed genes (DEGs). DEGs were selected using the thresholds |log$_2$(Fold Change)| > 1 and adjusted p-value (padjust) < 0.05. A volcano plot (Fig. 9A) visually summarizes the overall distribution of gene expression changes between the DSS model group and the healthy control group, as well as between the MCG

treatment group and the DSS model group. Comparative analysis between the IBD group and the IBD + MCG group revealed that MCG treatment reversed the abnormal expression of a substantial number of genes. A total of 29 significant DEGs were identified, of which 9 were significantly downregulated and 20 were significantly upregulated. This indicates that MCG treatment can broadly correct the gene expression dysregulation induced by DSS.

To analyze the expression changes of these significant DEGs in the IBD model group *versus* the MCG treatment group, a gene expression heatmap was generated (Fig. 9B). The heatmap was
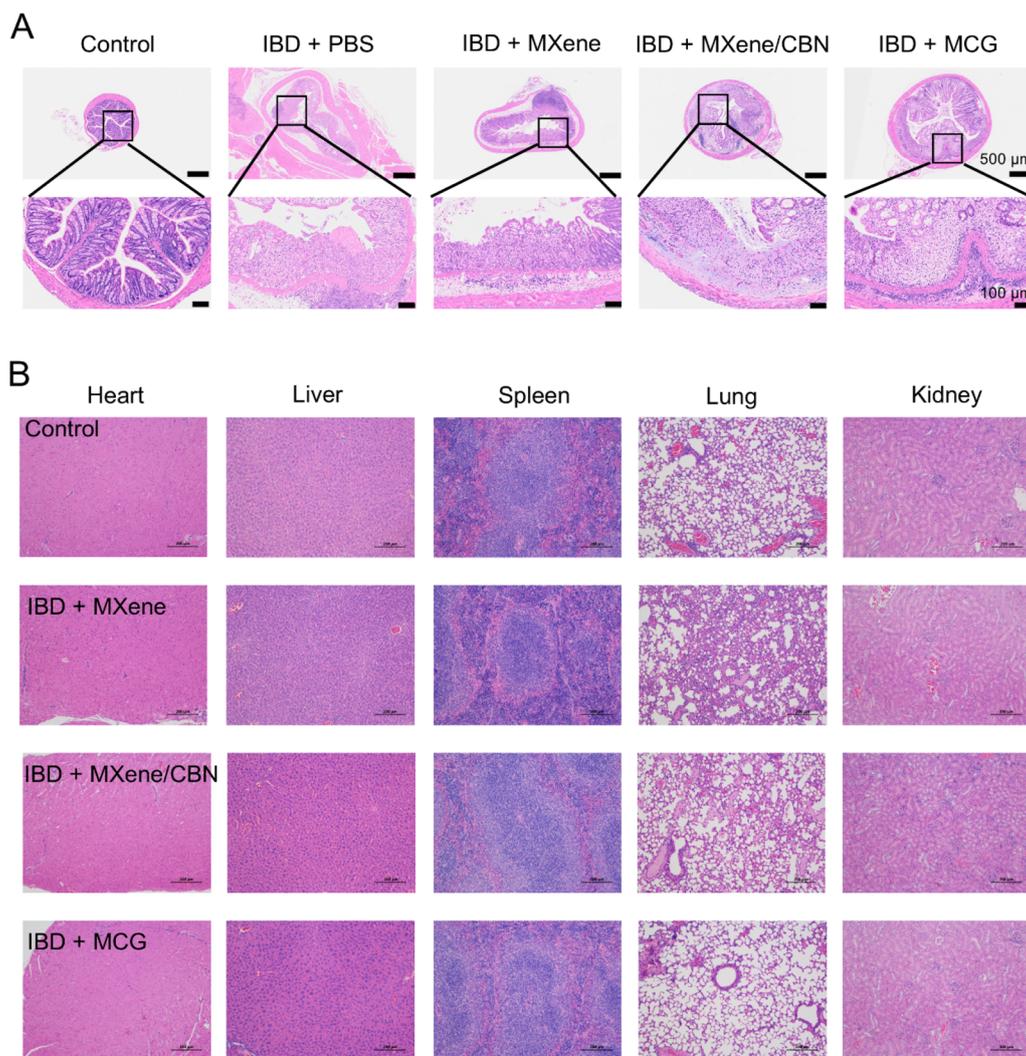
Fig. 8 (A) Representative images of H&E histological stain sections. Scale bar: 500 and 100 μm. (B) H&E histological stain sections of major organs (heart, liver, spleen, lung, kidney) scale bar: 200 μm.

visualized based on standardized expression values (Z-score), with red indicating high expression and blue indicating low expression. Sample clustering dendrograms were used to categorize samples and explore heterogeneity in gene expression and similarities between groups. Genes highly expressed in the IBD group, such as *Ces2h*, *H$_2$-T$_{22}$*, *H$_2$-T$_{23}$*, *Trim$_5$*, and *Tm$_{4sf5}$*, were significantly downregulated in the MCG group. Conversely, genes upregulated in the MCG group, including *Slc15a2*, *Cyp2f2*, *Casp14*, *St8sia5*, and *Zfp991*, suggest that MCG may alleviate inflammatory responses, enhance antioxidant capacity, and promote epithelial repair through regulating the expression of these genes. The heatmap revealed that multiple DEGs are highly associated with core pathways in IBD pathogenesis, including immune activation, epithelial injury, oxidative stress, and metabolic disturbance, providing important clues for elucidating the intervention mechanism of MCG and laying a foundation for subsequent mechanistic studies and target validation.

Kyoto Encyclopedia of Genes and Genomes (KEGG) pathway enrichment analysis was performed on the identified DEGs (Fig. 9C). The results showed that the significantly enriched pathways were primarily concentrated in immune- and inflammation-related biological processes. For instance, pathways such as "Cell adhesion molecules (CAMs)", "Human immunodeficiency virus 1 infection", "Allograft rejection", and "Graft-versus-host disease" were significantly enriched. The enrichment of the cell adhesion molecules pathway, in particular, indicates that these molecules may play a crucial role in the histopathological damage associated with IBD, specifically in regulating immune cell infiltration, barrier disruption, and signal transduction. Furthermore, pathways representative of classical autoimmune diseases, such as "Type I diabetes mellitus" and "Autoimmune thyroid disease", were also significantly enriched, implying potential shared immune mechanisms and gene expression patterns among these diseases.[11]
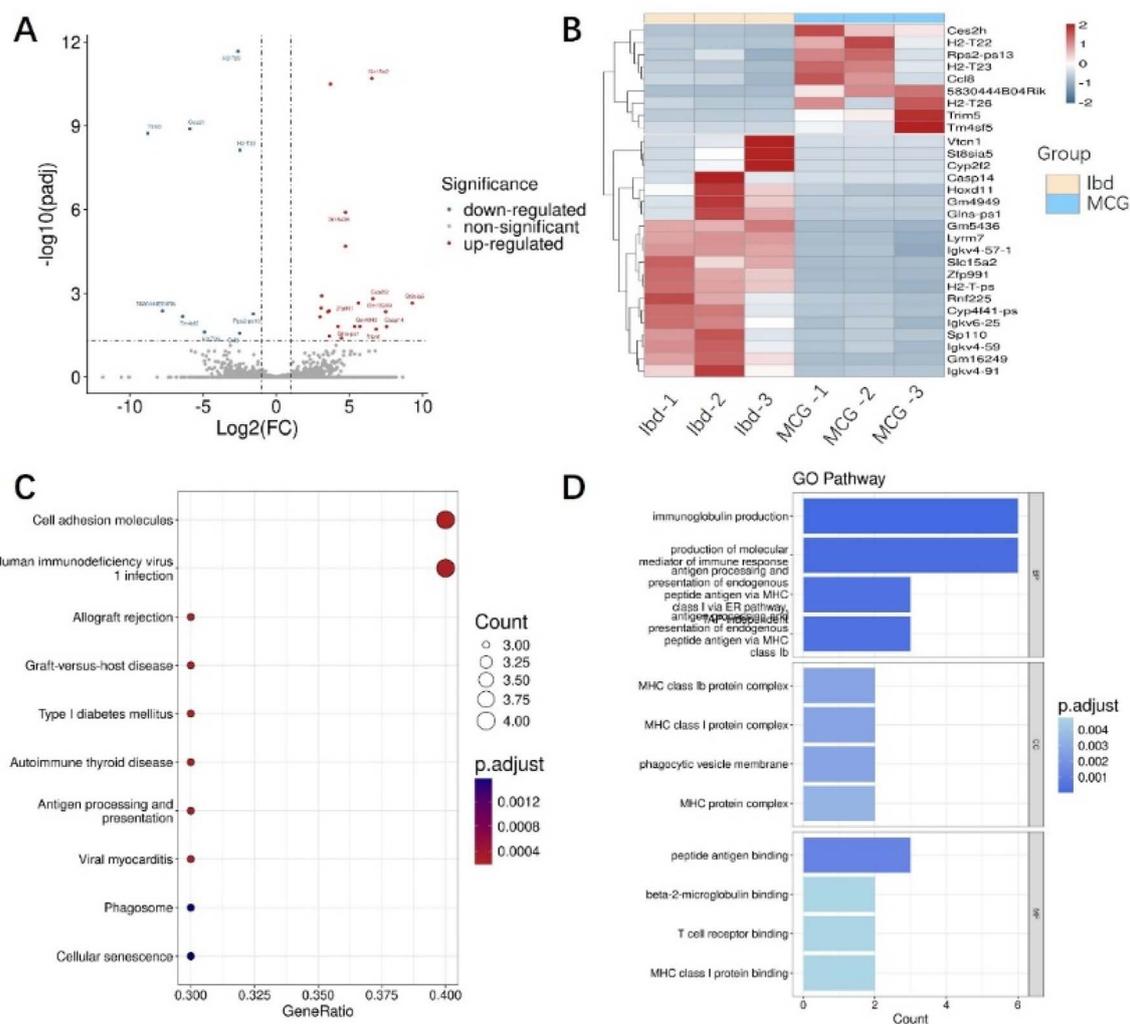
Fig. 9 (A) Presentation of volcano plots between different groups; (B) presentation of thermograms between different groups; (C) KEGG plots; (D) GO enrichment plots.

We further analyzed the functional enrichment of the DEGs in the Gene Ontology (GO) database, covering three categories: Biological Process (BP), Cellular Component (CC), and Molecular Function (MF) (Fig. 9D). Within Biological Processes, the most significantly enriched terms were "immunoglobulin production" and "production of molecular mediator of immune response", indicating that these differentially expressed genes are involved in the regulation of humoral immunity and the release of inflammatory factors. In summary, the GO analysis further validated the results from the KEGG analysis, demonstrating that in the IBD model, the differentially expressed genes are significantly enriched in immune-related pathways such as inflammation mediation, antigen recognition, phagocytosis, and immunoglobulin production. This suggests that the occurrence and progression of IBD are closely associated with dysregulation of both innate and adaptive immune responses.

To further investigate the biological functions of differentially expressed genes in the IBD mouse model, we performed Gene Set Enrichment Analysis (GSEA) against the Gene Ontology (GO) database (Fig. S8A and B). The results revealed significant upregulation or downregulation of multiple GO biological process pathways in the IBD group, indicating their potential critical roles in disease pathogenesis. Specifically, among the upregulated GO pathways, "immunoglobulin production" exhibited the highest level of enrichment, suggesting a hyperactivated adaptive immune response related to immunoglobulins in the IBD state. In contrast, among the downregulated pathways, the "ribonucleoprotein complex" pathway showed negative enrichment (NES < 0), indicating its significant suppression in the IBD group. Ribonucleoprotein complexes are involved in RNA splicing, stability maintenance, and post-transcriptional regulation; their downregulation may be closely associated with pathological alterations such as intestinal epithelial cell dysfunction and impaired protein synthesis.[31]

We also conducted KEGG pathway analysis on the differentially expressed genes (Fig. S8C and D). Among the

downregulated genes, the "cytokine–cytokine receptor interaction" pathway was significantly enriched, suggesting possible inhibition of this pathway in the IBD disease state. This pathway is closely associated with inflammatory cytokines (*e.g.*, IL-1β, TNF-α, IL-6, CXCLs), which play central roles in inflammatory cell infiltration, epithelial barrier disruption, and mucosal immune responses. Thus, the significant enrichment of this pathway further demonstrates that our model effectively recapitulates the inflammatory microenvironment of IBD. Meanwhile, the "calcium signaling pathway" showed a strong enrichment trend among the upregulated genes. Calcium ions play important roles in intracellular signal transduction, immune cell activation, and apoptosis.

In summary, the GSEA results reveal a coordinated mechanism involving immune response-related genes in the pathogenesis of IBD.

4. Conclusions

MCG, a nanozyme complex system with potent antioxidant, anti-inflammatory, and mucosal repair functions was successfully developed. Its therapeutic efficacy and mechanisms of action for IBD were systematically evaluated at molecular, cellular, and animal levels. The findings not only validated the composite system's promising therapeutic potential but more critically revealed a novel therapeutic paradigm involving multi-pathway, multi-target synergistic effects. This provides new insights and experimental evidence for localized targeted therapy of IBD.

Author contributions

Yanping Zhang: investigation, methodology, validation, data curation, formal analysis, writing – original draft. Hong Xi, Dongyuan Qin, Ping Cao: methodology, data curation, formal analysis. Shuo Yang, Jing Yin: methodology, vali dation. Tianliang Li: review, validation. Lili Ding: conceptualization, supervision, review and editing, funding acquisition, project administration.

Conflicts of interest

The authors declare that they have no known competing financial interests or personal relationships that could have appeared to influence the work reported in this paper.

Data availability

The authors declare that all relevant data supporting the findings of this study is available within the paper, the supplementary information (SI), and source data. Source data are provided with this paper. Supplementary information is available. See DOI: https://doi.org/10.1039/d5ra08772d.

Acknowledgements

Notes and references

1 Y. Pu, S. Huang, S. Gao, Y. Duan, W. Li, Q. Li, H. Lin, K. Zhang, M. Zhou and W. Wu, Cerium single-atom catalysts-armed Lactobacillus reuteri for multipronged anti-inflammatory/anti-fibrotic therapy of inflammatory bowel disease, *Acta Pharm. Sin. B*, 2025, **15**(10), 5400–5415.

2 Z. Z. Zhang, Y. Pan, Z. Y. Guo, X. Fan, Q. Q. Pan, W. X. Gao, K. Luo, Y. J. Pu and B. He, An olsalazine nanoneedle-embedded inulin hydrogel reshapes intestinal homeostasis in inflammatory bowel disease, *Bioact. Mater.*, 2024, **33**, 71–84.

3 J. Yao, J. Chen, L. Zhang, Y. Cheng, Z. Chen, Y. Zhang, X. Zheng, Y. Lv, S. Wang, Z. Li and J. Zhao, pH-responsive CuS/DSF/EL/PVP nanoplatform alleviates inflammatory bowel disease in mice *via* regulating gut immunity and microbiota, *Acta Biomater.*, 2024, **178**, 265–286.

4 D. C. Baumgart and S. R. Carding, Inflammatory bowel disease: cause and immunobiology, *Lancet*, 2007, **369**(9573), 1627–1640.

5 G. Han, H. Kim, H. Jang, E. S. Kim, S. H. Kim and Y. Yang, Oral TNF-α siRNA delivery *via* milk-derived exosomes for effective treatment of inflammatory bowel disease, *Bioact. Mater.*, 2024, **34**, 138–149.

6 Z. Fang, S. Zhang, W. Wang, Y. Xu, M. Lu, Y. Qian, X. Xiao, Y. Li, B. Z. Tang and M. Zhang, Aggregation-induced emission-based phototheranostics to combat bacterial infection at wound sites: a review, *Biomaterials*, 2024, **315**, 122950.

7 Y. Cui, D. Yang, Q. Li, Z. Peng, Z. Zhong, Y. Song, Q. Han and Y. Yang, Cu, Zn, I-Doped Carbon Dots with Boosted Triple Antioxidant Nanozyme Activity for Treatment of DSS-Induced Colitis, *ACS Appl. Mater. Interfaces*, 2024, **16**(25), 32619–32632.

8 J. Lloyd-Price, C. Arze, A. N. Ananthakrishnan, M. Schirmer, J. Avila-Pacheco, T. W. Poon, E. Andrews, N. J. Ajami, K. S. Bonham, C. J. Brislawn, D. Casero, H. Courtney, A. Gonzalez, T. G. Graeber, A. B. Hall, K. Lake, C. J. Landers, H. Mallick, D. R. Plichta, M. Prasad, G. Rahnavard, J. Sauk, D. Shungin, Y. Vazquez-Baeza, R. A. White 3rd, I. Investigators, J. Braun, L. A. Denson, J. K. Jansson, R. Knight, S. Kugathasan, D. P. B. McGovern, J. F. Petrosino, T. S. Stappenbeck, H. S. Winter, C. B. Clish, E. A. Franzosa, H. Vlamakis, R. J. Xavier and C. Huttenhower, Multi-omics of the gut microbial

ecosystem in inflammatory bowel diseases, *Nature*, 2019, **569**(7758), 655–662.

9 L. Larsen, A. Karachalia Sandri, J. Fallingborg, B. A. Jacobsen, H. A. Jacobsen, M. Bogsted, A. M. Drewes and T. Jess, Has the Incidence of Inflammatory Bowel Disease Peaked? Evidence From the Population-Based NorDIBD Cohort 1978–2020, *Am. J. Gastroenterol.*, 2023, **118**(3), 501–510.

10 Q. Wang, C. Cheng, S. Zhao, Q. Liu, Y. Zhang, W. Liu, X. Zhao, H. Zhang, J. Pu, S. Zhang, H. Zhang, Y. Du and H. Wei, A Valence-Engineered Self-Cascading Antioxidant Nanozyme for the Therapy of Inflammatory Bowel Disease, *Angew. Chem., Int. Ed.*, 2022, **61**(27), e202201101.

11 T. Li, Z. Wang, Z. Wang, Y. Pu, L. Lin, Z. Li, L. Chen, X. Liu, B. Cao, Y. Chen, Z. Li, Z. He, Y. Bai and L. Feng, "Three-birds, one-stone" biomimetic nanozyme system based on oxygen vacancy structure-regulated cascade reaction for inflammatory bowel disease, *Chem.–Eng. J.*, 2025, **512**, 162172.

12 Y. P. Zhang, P. Cao, D. Y. Qin, Y. Zhao, X. Chen and P. Ma, Anti-inflammatory, anti-colitis, and antioxidant effects of columbianadin against DSS-induced ulcerative colitis in rats *via* alteration of HO-1/Nrf2 and TLR4-NF-κB signaling pathway, *Inflammopharmacology*, 2025, **33**(1), 341–352.

13 T. L. Li, B. Cao, T. H. Su, L. X. Lin, D. Wang, X. T. Liu, H. Y. Wan, H. W. Ji, Z. X. He, Y. Y. Chen, L. Y. Feng and T. Y. Zhang, Machine Learning-Engineered Nanozyme System for Synergistic Anti-Tumor Ferroptosis/Apoptosis Therapy, *Small*, 2025, **21**(5), 2408750.

14 Y. Z. Zhang and Y. Y. Li, Inflammatory bowel disease: Pathogenesis, *World J. Gastroenterol.*, 2014, **20**(1), 91–99.

15 Q. Wang, C. Cheng, S. Zhao, Q. Liu, Y. Zhang, W. Liu, X. Zhao, H. Zhang, J. Pu, S. Zhang, H. Zhang, Y. Du and H. Wei, A Valence-Engineered Self-Cascading Antioxidant Nanozyme for the Therapy of Inflammatory Bowel Disease, *Angew Chem. Int. Ed. Engl.*, 2022, **61**(27), e202201101.

16 C. Cheng, S. Zhao, Y. Cheng, Y. Liu and H. Wei, Design of nanozymes for inflammatory bowel disease therapy, *Sci. China Life Sci.*, 2021, **64**(8), 1368–1371.

17 S. Zhao, Y. Li, Q. Liu, S. Li, Y. Cheng, C. Cheng, Z. Sun, Y. Du, C. J. Butch and H. Wei, An Orally Administered CeO$_2$@Montmorillonite Nanozyme Targets Inflammation for Inflammatory Bowel Disease Therapy, *Adv. Funct. Mater.*, 2020, **30**(45), 2004692.

18 Y. Chen, M. J. Shui, Q. Yuan, C. T. Vong, Z. M. Yang, Z. J. Chen and S. P. Wang, Wielding the double-edged sword: Redox drug delivery systems for inflammatory bowel disease, *J. Controlled Release*, 2023, **358**, 510–540.

19 X. J. Zeng, C. Zhao, X. Jiang, R. H. Yu and R. C. Che, Functional Tailoring of Multi-Dimensional Pure MXene Nanostructures for Significantly Accelerated Electromagnetic Wave Absorption, *Small*, 2023, **19**(41), 2303393.

20 J. Tan, J. H. Li and X. L. Zhou, The crystallization properties of antifreeze GelMA hydrogel and its application in cryopreservation of tissue-engineered skin constructs, *J. Biomed. Mater. Res.*, 2024, **112**(5), e35408.

21 J. Tan, J. H. Li and X. L. Zhou, Generation of cell-laden GelMA microspheres using microfluidic chip and its cryopreservation method, *Biomed. Mater.*, 2023, **18**(5), 055023.

22 Y. Chen, B. Guo, Y. Q. Zhang, X. Y. Bao, D. Li and J. Lin, Injectable hypoxia-preconditioned human exfoliated deciduous teeth stem cells encapsulated within GelMA-AMP microspheres for bone regeneration in periodontitis, *Colloids Surf., B*, 2025, **247**, 114452.

23 K. Y. Wong, Z. Y. Nie, M. S. Wong, Y. Wang and J. W. Liu, Metal-Drug Coordination Nanoparticles and Hydrogels for Enhanced Delivery, *Adv. Mater.*, 2024, **36**(26), 2404053.

24 M. L. Tang, Y. T. Shi, L. Lu, J. Q. Li, Z. C. Zhang, J. T. Ni, W. X. Wang, Y. H. Zhang, T. D. Sun and Z. G. Wu, Dual active nanozyme-loaded MXene enables hyperthermia-enhanced tumor nanocatalytic therapy, *Chem. Eng. J.*, 2022, **449**, 137847.

25 H. Yao, F. Wang, H. Chong, J. Wang, Y. Bai, M. Du, X. Yuan, X. Yang, M. Wu, Y. Li and H. Pang, A Curcumin-Modified Coordination Polymers with ROS Scavenging and Macrophage Phenotype Regulating Properties for Efficient Ulcerative Colitis Treatment, *Adv. Sci.*, 2023, **10**(19), e2300601.

26 X. C. Morgan, T. L. Tickle, H. Sokol, D. Gevers, K. L. Devaney, D. V. Ward, J. A. Reyes, S. A. Shah, N. LeLeiko, S. B. Snapper, A. Bousvaros, J. Korzenik, B. E. Sands, R. J. Xavier and C. Huttenhower, Dysfunction of the intestinal microbiome in inflammatory bowel disease and treatment, *Genome Biol.*, 2012, **13**(9), R79.

27 X. Wang, M. He, Y. Zhao, J. He, J. Huang, L. Zhang, Z. Xu, Y. Kang and P. Xue, Bimetallic PtPd Atomic Clusters as Apoptosis/Ferroptosis Inducers for Antineoplastic Therapy through Heterogeneous Catalytic Processes, *ACS Nano*, 2024, **18**(11), 8083–8098.

28 Z. Shi, X. Li, J. Chen, Z. Dai, Y. Zhu, T. Wu, Q. Liu, H. Qin, Y. Zhang and H. Chen, Enzyme-like biomimetic oral-agent enabling modulating gut microbiota and restoring redox homeostasis to treat inflammatory bowel disease, *Bioact. Mater.*, 2024, **35**, 167–180.

29 J. Wu, X. Zhu, Q. Li, Q. Fu, B. Wang, B. Li, S. Wang, Q. Chang, H. Xiang, C. Ye, Q. Li, L. Huang, Y. Liang, D. Wang, Y. Zhao and Y. Li, Enhancing radiation-resistance and peroxidase-like activity of single-atom copper nanozyme *via* local coordination manipulation, *Nat. Commun.*, 2024, **15**(1), 6174.

30 Y. Wang, Y. Zhang, Y. P. Yang, M. Y. Jin, S. Huang, Z. M. Zhuang, T. Zhang, L. L. Cao, X. Y. Lin, J. Chen, Y. Z. Du, J. Chen and W. Q. Tan, Versatile dopamine-functionalized hyaluronic acid-recombinant human collagen hydrogel promoting diabetic wound healing *via* inflammation control and vascularization tissue regeneration, *Bioact. Mater.*, 2024, **35**, 330–345.

31 Q. J. Ren, S. Sun and X. D. Zhang, Redox-active nanoparticles for inflammatory bowel disease, *Nano Res.*, 2021, **14**(8), 2535–2557.